

Experiments on nonlinear instabilities and evolution of steep gravity-wave trains

By MING-YANG SU, MARK BERGIN, PAUL MARLER
AND RICHARD MYRICK

Naval Ocean Research and Development Activity, NSTL Station, Mississippi 39529

(Received 23 September 1981 and in revised form 20 April 1982)

A series of experiments on strong nonlinear instabilities of gravity-wave trains of large steepness $0.25 \leq ak \leq 0.34$ in deep water in a long tow tank and a wide basin were performed. These experiments clarified several phenomena such as subharmonic instabilities, wave breaking, evolution of power spectra and directional energy spreading. It was found that an initial two-dimensional wavetrain of large steepness evolved into a series of three-dimensional spilling breakers, and was followed by a transition to a two-dimensional modulated wave train during which a series of oblique wave groups were radiated. The final stage of evolution was a series of modulated, two-dimensional wave groups with lower steepness and frequency. The three most frequent normal modes of two-dimensional subharmonic instabilities underlying the frequency downshifting, in the order of their relative occurrence, are found to be about $4/3$, $5/4$ and $3/2$ in terms of the ratio of the fundamental to perturbed wave frequencies. The timescale for the phenomenon of the frequency downshifting is from 40 to 60 fundamental wave periods. Comparisons of the experimental results with existing theories showed that observed processes have several qualitative similarities with theoretical computations.

1. Introduction

Recently, much attention has been given to the problems of instability and evolution of water waves of finite steepness. For a Stokes wave train of small (but finite) steepness, Benjamin & Feir (1967) discovered a sideband instability, which was confirmed experimentally (Feir 1967). The long-time evolution of a two-dimensional wave train after the initial instability of Benjamin–Feir type was investigated experimentally by Lake *et al.* (1977). They concluded that the instability did not lead to wave-train disintegration, but instead exhibited the similarity of the Fermi–Pasta–Ulam recurrence.

For finite-amplitude wave trains, a comprehensive, two-dimensional linear stability analysis was given by Longuet-Higgins (1978*a, b*), who considered normal-mode perturbations (both subharmonic and superharmonic) of wave trains of arbitrary steepness. He showed that, as the steepness ak (a denotes amplitude and k wavenumber) increases, the perturbation becomes unstable until ak reaches 0.346, at which value stability is regained. He also found that, at values of ak near 0.41, a new type of instability appears with a much higher growth rate. Concurrently, Longuet-Higgins & Cokelet (1976, 1978) made accurate numerical computations of the evolution of steep two-dimensional wave trains. In the two examples computed at initial wave steepness $ak = 0.25$ and 0.32 respectively these computations show that the subharmonic instabilities ultimately cause every alternate crest to develop a fast-growing local instability that quickly leads to wave breaking of the plunging type.

McLean *et al.* (1981) and McLean (1982*a*) showed that there are two main types of instabilities, designated as types I and II respectively. Type I are the subharmonic instabilities, first discovered by Benjamin & Feir (1967), which occur roughly in the range $0 < ak < 0.38$. Type II are the much faster-growing instabilities that were first discovered by Longuet-Higgins (1978*a, b*) in the two-dimensional case, when $ak \geq 0.40$. McLean *et al.* (1981) show further that there are some three-dimensional instabilities of type II, continuous with the two-dimensional type II instabilities when $ak \geq 0.40$, but which also exist at all lower values of ak .

The purpose of this paper is to report the findings of experiments on the evolution of initially two-dimensional steep gravity-wave trains in deep water. These experiments were performed in a tow tank and a large outdoor basin. Results were very similar in both cases. For the values of steepness of wave trains in the range of $0.25 \leq ak \leq 0.34$, it is found that the subharmonic instabilities cause alternate crests to develop a relatively fast-growing local instability, leading to near breaking. This three-dimensional characteristic of wave evolution is qualitatively consistent with the type II instability when $ak > 0.30$ (McLean *et al.* 1981; McLean 1982*a*). At a later stage these crescent-shaped breakers disappear and the wave field returns to a series of essentially two-dimensional wave groups with peak frequency and wave slope that are significantly lower than those of the initial wave train.

In §2, the experiments in the tow tank and the wide basin will be described in detail. Results are presented for the tow tank in §3 and for the wave basin in §4. Comparisons with theoretical predictions and discussions will be given in §5. Conclusions are summarized in §6.

2. Experiments

Experiments were performed in two different facilities, the indoor tow tank and the outdoor wave basin at Naval Ocean Research and Development Activity (NORDA). These experiments are described separately below.

2.1. Experiments in the tow tank

2.1.1. *The tow (wave) tank.* Experiments were conducted in a $3.7 \times 3.7 \times 137.2$ m tow tank, which is equipped with a computer-controlled carriage (figure 1) that has a maximum speed of 4.5 m/s. The carriage is instrumented to provide automatic printout of elapsed travel time and distance.

2.1.2. *The wavemaker.* The wavemaker is of a plunger type with a crest length of 3.66 m. Two types of plungers were used. The forward face of plunger A (figure 1*b*) is an approximation to a hyperbola consisting of three joined flat surfaces. The forward face of plunger B (figure 1*b*) is a continuous hyperbolic curve. An explanation of the use of the two plunger configurations will be discussed in §3. The wavemaker operates over a frequency range 0.5–2.0 Hz, and the maximum stroke available is 30.5 cm.

2.1.3. *Wave-height sensors.* The wave-height sensors detect changes in capacitance caused by fluctuations in water level. The sensor element is a single, double-coated magnet wire with a diameter of 0.5 mm. The electronic circuitry converts the variations in capacitance caused by water-surface displacements into a d.c. voltage proportional to surface displacement. The design of the sensor is presented in Hsu (1976). These sensors have several attractive advantages over other types: (i) the response is linear; (ii) it is easily tuned for maximum sensitivity over a wide range

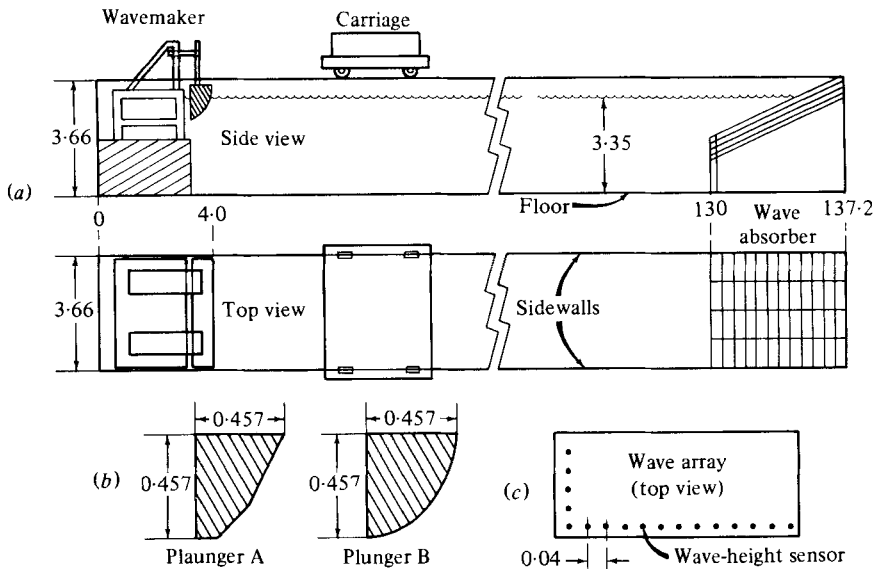


FIGURE 1. Indoor tow-tank facility: (a) major dimension of the tow tank and arrangement; (b) two plungers A and B; (c) array board for wave-height sensors. Lengths are in m.

of wave heights; (iii) it is compact and easily fabricated owing to the use of integrated circuits. Sets of these sensors can be arranged in arbitrary patterns as required.

2.1.4. *Data-acquisition system.* The data-acquisition system is designed specifically for wave-current interaction studies. It is equipped to process up to 20 wave-height sensor outputs, 20 current meters, 3 components of wind velocity, the period of the wavemaker and two miscellaneous inputs. Wave-height records are filtered with a 3 dB roll-off at 40 Hz and are digitized with a 12-bit accuracy at 40 samples per second. The digitized data are formatted and stored on a 9-track tape recorder. Up to 10 selectable channels of wave heights or current data may be printed concurrently with these records at a data terminal, which is used for monitoring measurements in progress. Four channels of 12-bit digital/analog conversion are available as inputs to an oscillograph, oscilloscope, or analog spectrum analyser.

2.1.5. *Probe calibration.* The wave probes are calibrated before and after each daily measurement cycle. Very little drift in the calibrations has been observed to occur over the usual 8 h measurement periods. Consequently, the first calibration is normally used for most measurements, and the second furnishes a check on the overall system performance. The period of the wave plunger is measured at the drive shaft.

2.1.6. *Wave reflections.* The wave absorber at the end of the tow tank has an absorption efficiency of about 80%; consequently the duration of an experiment is limited to a period during which no significant contamination by the reflection of waves from the end of the tank occurs. Owing to the length of the tank the experiments are not severely curtailed by this restriction. Measurements from an initial calm state can be obtained up to about 110 m from the wave plunger without significant contamination by reflected waves. A settling time of approximately 15 minutes between two successive measurement periods is sufficient for the tank to become calm.

2.1.7. *Data analysis and display.* Wave-amplitude spectra are computed using standard time-series analysis programs on a CDC 6600 computer, or near-real-time

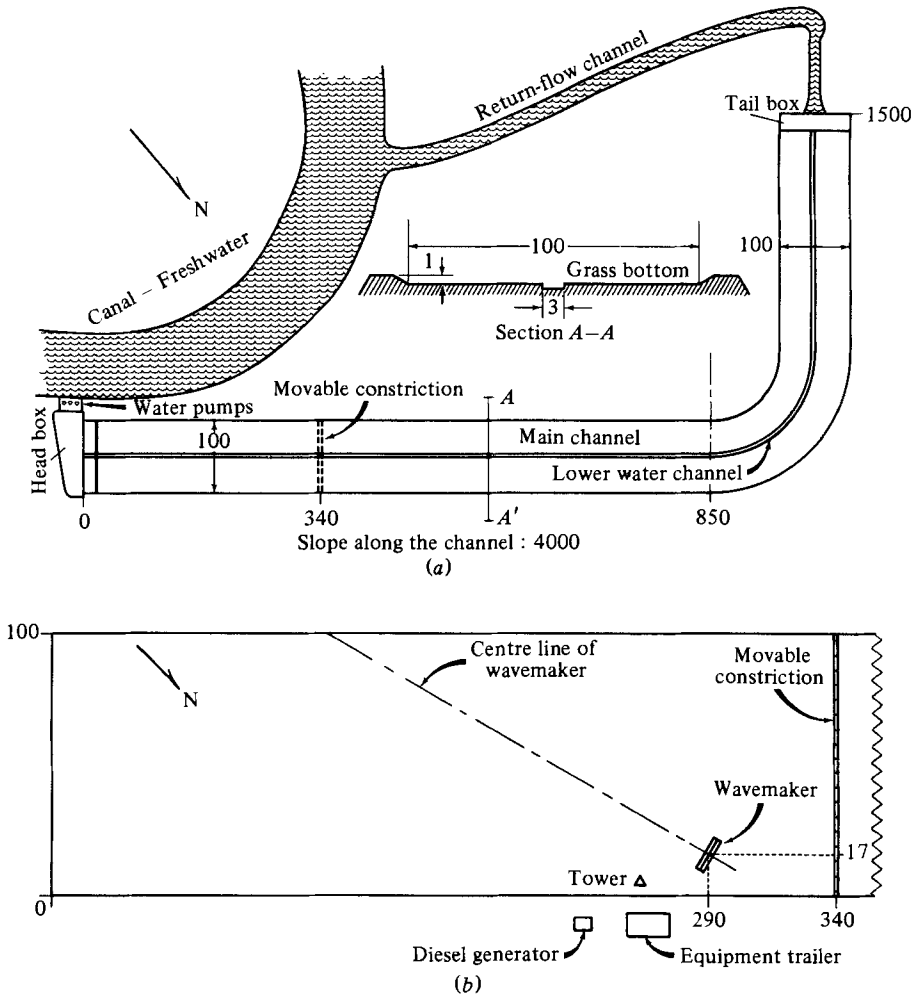


FIGURE 2. Outdoor experimental facility: (a) wave-current interaction channel; (b) the wave basin and location of the wavemaker. Lengths are in m.

spectral analyses can be performed on an analog spectrum analyser that has internal fast-Fourier-transform digital processing. The time series of wave displacements are displayed on an oscillograph, which receives inputs from the wave probes or from the recorded digital tapes through digital/analog converters.

2.2. Experiments at the wide basin

2.2.1. The wide basin. The general layout of the basin is shown in figure 2. It is L-shaped and is 1 m deep, 100 m wide and 1500 m long. It has a grass bottom, which is mowed regularly to any desired height. Three centrifugal pumps with a combined maximum discharge rate of $6 \text{ m}^3/\text{s}$ can generate a continuous flow in the basin. At the location 340 m downstream from the head box, a movable constriction (1 m high), which consists of 30 separate connecting gates each 3.33 m long, can be used to produce various flow constrictions.

For our present experiments in still water, the constriction is completely closed to create a constant-depth basin 100 m by 340 m. The location and orientation of the

wavemaker in the channel is shown in the enlarged section (figure 2*b*). The wavemaker is oriented so that a wave train may propagate on the left side (seen from the centre of the wavemaker) to the greatest distance in the channel at the expense of the wave train propagating on the right side. The wave on the right side will be affected earlier by the reflected waves from the banks.

Before each series of experiments, the channel bottom is mowed so that the grass is less than 5 cm high. The normal water depth for all cases described here is 80 cm above the top of the grass. The wavelengths used were less than 1.30 m for the water wave under study. Thus the waves are effectively in deep water so far as the fundamental and superharmonic instabilities are concerned, but not necessarily as regards the subharmonic instabilities, which have greater wavelengths (§3). However, comparisons between the experimental results in the wide basin with those in the tow tank, which has a depth greater than 3 m, show little finite-depth effects (§§4 and 5). Furthermore, McLean (1982*b*) has shown that, at the quoted wavelength-to-depth range, the finite-amplitude effect is negligible insofar as both type I and type II instabilities are concerned.

A rectangular grid of markers (sticks extending out of the water surface) with 6.1 m (20 ft) separation is also installed in front of the wavemaker. The x -axis is normal to the wavemaker, and the y -axis is parallel with the face of the plunger, the centre of which is the origin of the coordinate system.

2.2.2. *The wavemaker.* The mechanical wavemaker is of a plunger-type. The total (maximum) crest length is 15.8 m. It is composed of three separable sections of 6.1, 3.6 and 6.1 m respectively. Hence two other possible operating crest lengths are 3.6 and 9.7 m. The central section contains the driving motor and a variable-reduction gear box for controlling the wave period. The operating frequency range is 0.5–2.0 Hz. The cross-section of the plunger is the same as plunger A in figure 1. The normal operating still-water level is near the middle of the topmost flat face. The maximum stroke available for the plunger is 30.5 cm. The centre section of the wavemaker is the same as that at the wave tank. The wavemaker, which weighs about 5500 kg, is also equipped with a set of attachable floatation devices for easy transportation and rotation in the basin.

2.2.3. *The observation tower.* A 21 m high foldover tower is erected on the left side of the wavemaker to provide a vantage point for direct observations of overall wave patterns and as a platform for taking still and motion pictures. These pictures are found to be very helpful in the recording and subsequent studying of the rapidly changing three-dimensional wave motion.

2.2.4. *Other equipment.* The wave-height sensors, the data-acquisition system, and other data-processing equipment are the same as those used in the tow tank described in 2.1. During the experiment in the outdoor wave basin, the data-acquisition system and other electronic analysis equipment are housed in a trailer. A power supply of 440 V for the wavemaker and 110 V for other instruments is provided by a portable diesel power generator and transformer located adjacent to the trailer. Hence it is not too difficult to move the entire experimental setup to different locations of the large open basin.

2.2.5. *Experimental procedures.* The experiments were conducted by using two plunger strokes of 5.1 and 10.2 cm in conjunction with four wave periods from 0.78 to 1.0 s. These parameters of the wavemaker are the same as those in §2.1 and also satisfy the following constraints in the wave basin:

- (i) the generated waves are deep-water waves;
- (ii) the range of wave steepness is $0.20 \leq ak \leq 0.34$;

(iii) the strong wave interactions occur within 60 m of the wavemaker, so the wave pattern and its evolution can be measured and observed more easily;

(iv) the reflected waves from the banks of the channel do not interfere with the wave evolution during the measuring period.

Because the wave channel is in an open environment without cover, all the experiments were conducted during very calm times of the day when the wind speed is less than 0.5 m/s. In this locality, such calm situations often prevail in the early morning or late afternoon during the land/sea breeze transition. Our experimental situation and the size of facility lies between most smaller-scale indoor laboratories and large natural water bodies.

In these experiments on wave instabilities and evolution, we have concentrated on the general characterization of three-dimensional evolution of a steep wave train and wave profiles along a line normal to the centre of the wavemaker. Wave profiles are measured at eight stations with 6.1 m intervals. At each station, four surface displacements are measured by an array with four wave probes. The combination of no. 1 and no. 3 wave probes are used for measuring wavelength and phase speed. The combination of no. 2, no. 3 and no. 4 wave probes is used for determining cross-sections of the three-dimensional structure of the modulated wave train when it reaches its breaking stage.

In addition to recording all the wave-height data for detailed digital processing and analysis, real-time plots of selected portions of wave profiles are made using a four-channel oscillographic recorder. The frequency spectra are obtained by an analog spectrum analyser.

Both photographs and motion pictures of various stages of evolution of the wave train from different perspectives were also taken routinely during experiments. Careful examination of these pictures provides useful information and insight into the complicated three-dimensional phenomena.

3. Results of experiments in the wave tank

The dominant processes that control highly nonlinear evolution of deep-water gravity-wave trains depends mainly on initial wave steepness ak . First, we shall describe these characteristics using still photographs of wave patterns at various stages of evolution. This description will be followed by presentation of wave profiles measured along the centreline of the tow tank at 11 stations.

3.1. *General characteristics of the wave-train evolution*

As a typical case (case A), a wave train is generated by the wavemaker with the curved plunger B giving a wave amplitude of 3.3 cm and a period of 0.645 s. The initial frequency of the wave train is $f_0 = 1.55$ Hz with wavelength $\lambda_0 = 65$ cm and steepness $a_0 k_0 = 0.32$. Figure 3 shows the forward face of the plunger and the first five waves. Small modulations and capillary waves on these basic waves are initial transient disturbances. The details of these initial disturbances depend on the shape and vertical excursion of the plunger in addition to wave steepness. Thus we have purposely employed two different shapes of plungers, as shown in figure 1 (*b*). Plunger A, with an abrupt change between joined flat plates, should create more disturbances than the smooth plunger B. We found that, except in the proximity of the wavemaker ($x < 10\lambda_0$), the nonlinear evolution of wave trains demonstrates essentially the same modulational characteristics by using either of these two plungers. This finding is consistent with theoretical predictions, since the main variations in the disturbances

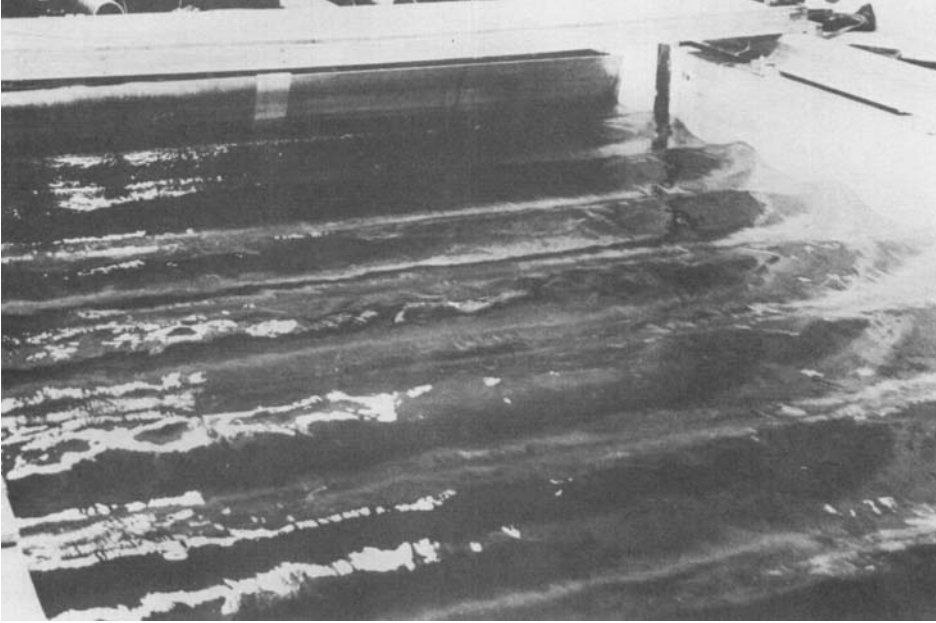


FIGURE 3. The wavemaker and initial waves in the tow tank; $f_0 = 1.55$ Hz, $(ak)_0 = 0.318$.



FIGURE 4. Three-dimensional spilling breakers at $x \approx 18$ m to $x \approx 25$ m.

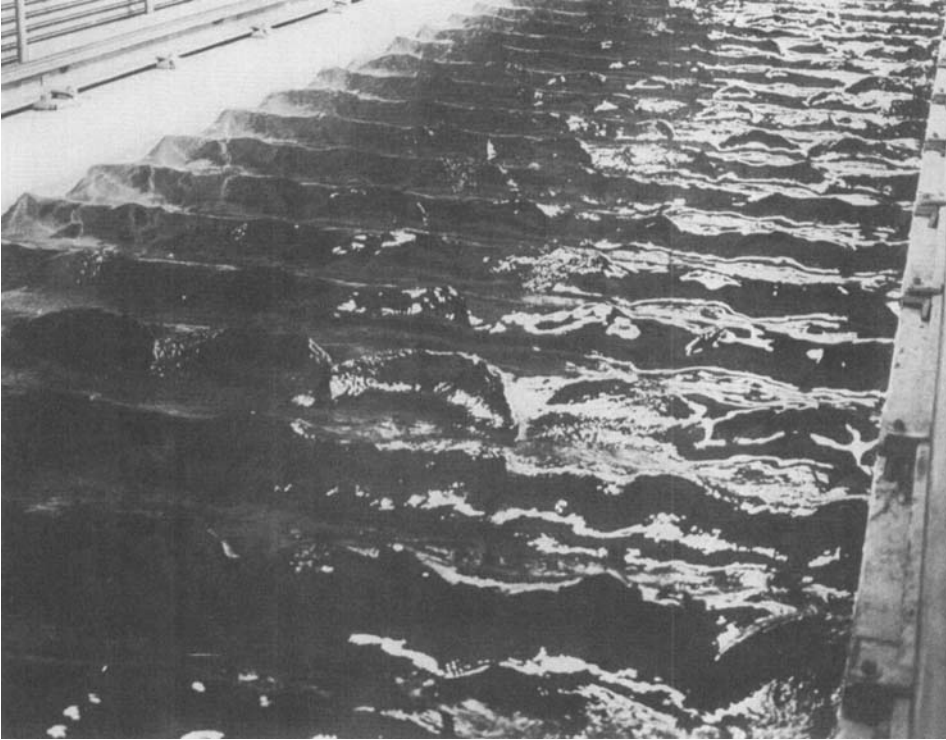


FIGURE 5. Close-up photograph of figure 4.

from different plungers will be superharmonic, which has a scale less than λ_0 , rather than subharmonic, which has a scale greater than λ_0 . The subharmonic disturbance is the main cause for the long-time evolution of nonlinear instabilities.

At around $x = 12.2$ m ($\approx 19\lambda_0$), which we consider as the first stage of wave evolution, some small-scale breaking occurs on wave crests. These small breaking waves appear to be the results of superharmonic instabilities. During the same period, the growth of subharmonic disturbances accelerates. From this distance to $x \approx 15.5$ m ($\approx 24\lambda_0$), transverse perturbation causes the wave train to evolve quickly into a three-dimensional configuration (foreground of figure 4), which shows a very regular arrangement of six crescent-shaped breaking waves per row with a cross-wave shift of one half-crescent between any two consecutive rows. That is, there are six whole breakers in one row, while there are five whole breakers and two half-breakers in the next row. Figure 5 shows a close-up view of these breakers; the central part of the crescent-shaped wave actually accelerates and spills over the front (or forward) face. Hence these are called spilling breakers. Some of this spilling also entrains air bubbles and appears as white-capping. (The appearance of each crescent-shaped wave resembles a spilling breaker in the open ocean.) Furthermore, two adjacent crescent-shaped waves on the same crest of the basic wave are seen to interact strongly, causing a substantial deepening in the trough of the underlying basic wave. The deepest part of the trough follows the highest part of the crescent-shaped wave. The combined effect of these two features increases the slope on the front face of the crescent-shaped wave along its axis of symmetry. The water surface between two adjacent crescent-shaped waves is lower than the initial wave train. Thus the nonlinear wave interaction



FIGURE 6. Two-dimensional wave forms after disappearance of spilling breakers.

produces a localized instability, which transforms an initially two-dimensional wave train into a three-dimensional unstable wave pattern with subharmonic structure in the direction of propagation of the basic wave. Ultimately, this leads to wave breaking. For this particular case, the crestwise length of the spilling breakers is 61 cm, and is slightly shorter than the initial 65 cm wavelength of the primary waves.

This second stage of evolution has a distinct three-dimensionality that usually lasts about 10 wavelengths, and is followed by the next stage in which the crescent-shaped breakers quickly disappear. The wave train returns to a more or less two-dimensional form, but with continuous modulations (figure 6). Finally, the wave train becomes a series of wave groups after about 40–60 wavelengths from the wavemaker. Each wave group contains roughly 6–8 waves.

3.2. Wave profiles

The observations of the general qualitative characteristics of wave evolution described in §3.1 will now be described more quantitatively by wave profiles measured at various distances away from the wavemaker. Figure 7 shows such wave profiles along the centreline of the tow tank from $x = 6.1$ m ($\approx 9\lambda_0$) to $x = 106.7$ m ($\approx 164\lambda_0$). The wave profile at $x = 6.1$ m ($\approx 9\lambda_0$) exhibits very slow and slight modulation with a periodicity of about six or more wavelengths. The wave profile at $x = 12.2$ m ($\approx 19\lambda_0$) shows more rapid modulations with obvious pairs of consecutive higher and lower waves. These types of subharmonic modulations intensify greatly in the next wave profile at $x = 15.25$ m ($\approx 24\lambda_0$), and continue to $x = 24.4$ m ($\approx 38\lambda_0$). These higher waves correspond to the three-dimensional spilling breakers. Figure 8(b) gives a sketch of the top view of the crescent-shaped breakers, while figure 8(a) shows a sketch of wave profiles associated with the breaker along its axis of symmetry.

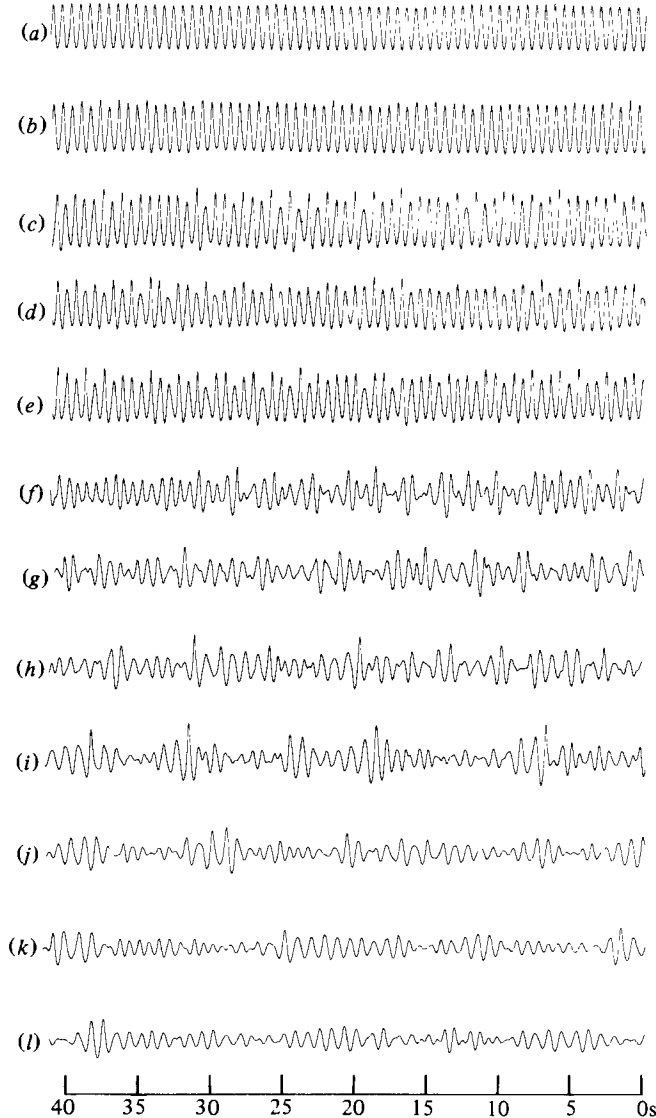


FIGURE 7. Wave profiles at various stages of evolution with $f_0 = 1.55$ Hz, $(ak)_0 = 0.318$; at locations from the wavemaker (a) 6.1 m; (b) 12.2 m; (c) 15.25 m; (d) 18.6 m; (e) 24.4 m; (f) 30.5 m; (g) 36.6 m; (h) 48.8 m; (i) 61.0 m; (j) 76.25 m; (k) 91.5 m; (l) 106.75 m.

The wave profiles have the following notable features:

- (i) the height of wave crest increases in alternate waves;
- (ii) the wave trough deepens in front of the following higher wave;
- (iii) the wavelength, which is measured between two consecutive wave troughs, is shorter for the higher wave than for the lower wave;
- (iv) the combined result of above three features yields the highest slope at the front face of the higher wave.

The average steepness for these breakers ($ak \approx 0.42$) is larger than the initial value ($ak = 0.32$), but is still smaller than that of the Stokes limiting waves ($ak = 0.446$). Since the breaking wave is asymmetric about its crest, and the troughs on either side

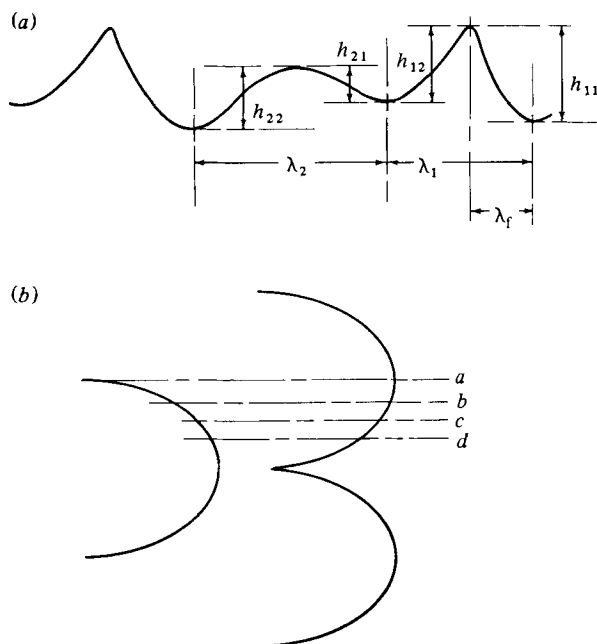


FIGURE 8. Definition sketch of three-dimensional spilling breakers: (a) wave profile along the symmetric axis of a spilling breaker; (b) top view.

are also at different depths, the above-average steepness ak is estimated using the average of the two heights of the wave crest with respect to both troughs. The distance between these two troughs is assumed to be the wavelength.

From $x = 30.5$ m ($\approx 47\lambda_0$) to $x = 36.6$ m ($\approx 56\lambda_0$), wave breaking usually occurs every third or every fourth wave. From $x = 48.8$ m ($\approx 75\lambda_0$) to 61.0 m ($\approx 94\lambda_0$), waves break less often. At this stage wave crests extend across the width of the tow tank. These breaking waves are nearly two-dimensional and are different in structure from the distinctly three-dimensional breakers occurring between $x = 18.6$ m ($\approx 29\lambda_0$) and $x = 24.4$ m ($\approx 38\lambda_0$).

As the wave train evolves further, near-breaking waves are observed only occasionally, and the distance between them also increases. Finally, the profiles at $x = 91.5$ m ($\approx 141\lambda_0$) and 106.75 m ($\approx 164\lambda_0$) exhibit modulational characteristics of a series of wave groups. The typical steepness of these waves is $ak \approx 0.15$, which is only about half the initial steepness $ak = 0.32$ at $x = 6.1$ m ($\approx 9\lambda_0$). Furthermore, it can be noted from these wave profiles that the average wave period is longer than the period at $x = 6.1$ m.

In summary, after strong nonlinear interactions, the initially two-dimensional wave train develops into a series of three-dimensional spilling breakers, and finally becomes a series of two-dimensional wave groups with significantly less steepness and lower frequencies.

3.3. Dependence of evolution on wave steepness

In order to examine effects of the initial wave steepness on the evolution of wave forms, we shall further present three cases designated as B, C and D with $a_0 k_0 = 0.25$, 0.30 and 0.33 respectively.

Case B ($f_0 = 1.05$ Hz and $a_0 k_0 = 0.25$) starts to show appreciable modulation after

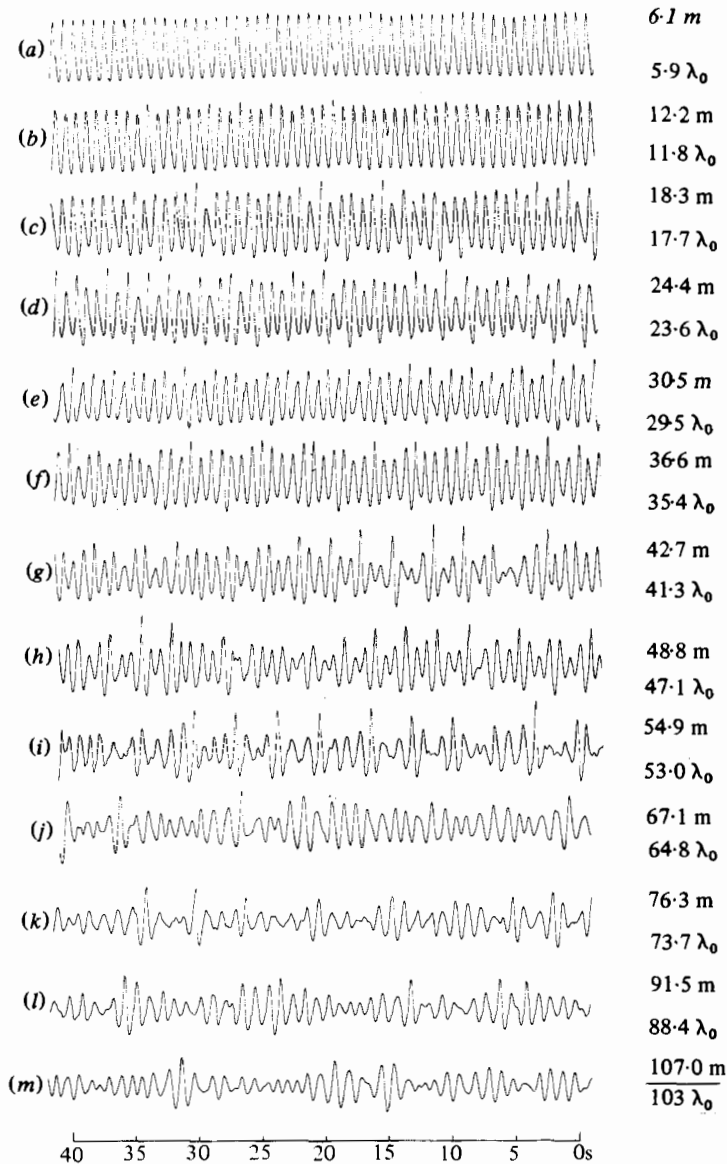


FIGURE 9. Evolution of wave profiles for case D; $f_0 = 1.25$ Hz, $\lambda_0 = 1.035$ m, $a_0 k_0 = 0.33$. Distance away from the wavemaker is (a) $x = 6.1$ m; (b) 12.2 m; (c) 18.3 m; (d) 24.4 m; (e) 30.5 m; (f) 36.6 m; (g) 42.7 m; (h) 48.8 m; (i) 54.9 m; (m) 106.7 m.

$x > 30.5$ m ($23.6\lambda_0$), and the strongest interaction around $x = 67.1$ m ($51.8\lambda_0$). Note that a substantial change occurs between $x = 54.9$ m ($42.4\lambda_0$) and $x = 67.1$ m; i.e. every four to five waves in the time domain tend to be extremely high and breaking. Some waves appear to 'vanish' between these highest waves.

Case C ($f_0 = 1.15$ Hz and $a_0 k_0 = 0.30$) starts to show significant modulation at $x = 24.4$ m ($21.6\lambda_0$), but the modulation patterns as exhibited in wave profiles from $x = 24.4$ m ($21.6\lambda_0$) to $x = 36.6$ m ($32.5\lambda_0$) are different from those in case B. For case C the most noticeable feature is that high and low crests alternate.

For the next wave profile at $x = 42.7$ m ($37.9\lambda_0$), which is only about 5 wavelengths

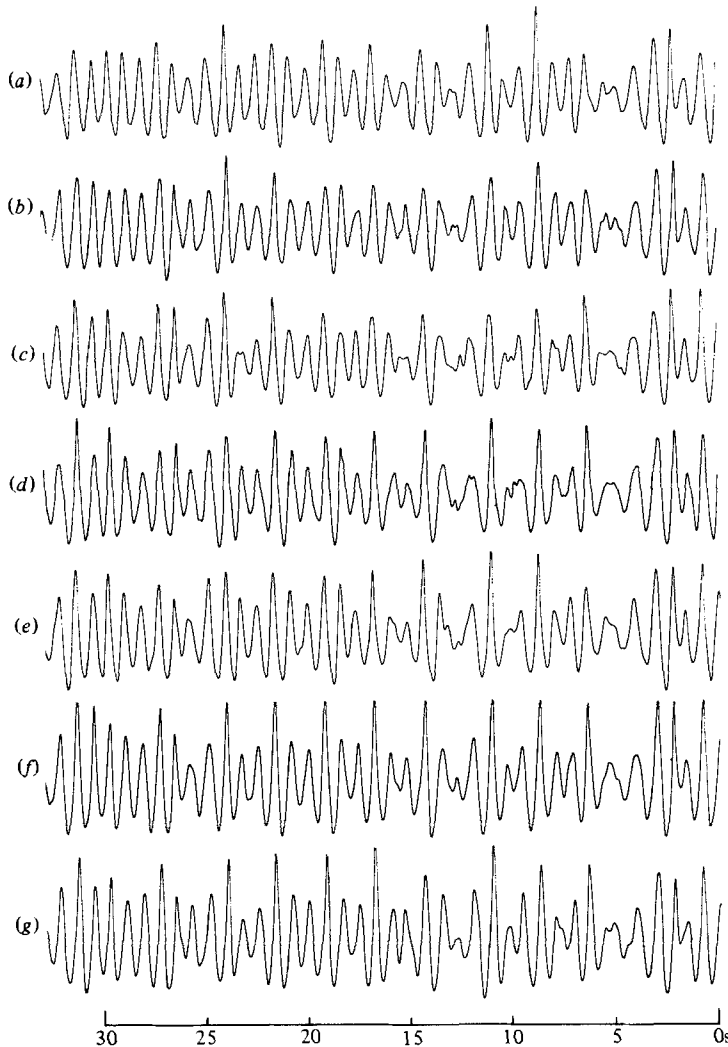


FIGURE 10. Wave profiles for case D at $x = 42.7$ m with (a), (b), ..., (g) given by $y = n\Delta y$, $n = 0, 1, \dots, 6$ and $\Delta y = 22.86$ cm.

downstream, the time-domain wave profile again shows the modulational characteristics similar to those observed in case B at $x = 48.8$ m ($37.7\lambda_0$). The wave profile at $x = 36.6$ m ($32.5\lambda_0$) in case C corresponds to that at $x = 67.1$ m ($51.8\lambda_0$) in case B. Now, starting at $x > 67.1$ m ($59.6\lambda_0$) in case C, the wave form quickly reconstitutes itself and becomes more or less uniform again, but with a lower frequency than the initial frequency at $x = 6.1$ m ($5.4\lambda_0$).

Case D ($f_0 = 1.25$ Hz and $a_0 k_0 = 0.33$, figure 9) shows many characteristics similar to case C, except that the strong modulations occur at shorter distances from the wavemaker.

In contrast to the strong modulation leading to three-dimensional wave breaking, the strong modulations resulting in low-frequency waves in cases B, C and D are essentially two-dimensional. These two-dimensional characteristics (measured at $x = 42.7$ m ($41.3\lambda_0$)) are demonstrated in figure 10 for case D; eight wave profiles are measured simultaneously at intervals of 22.86 cm, spanning half of the tank width.

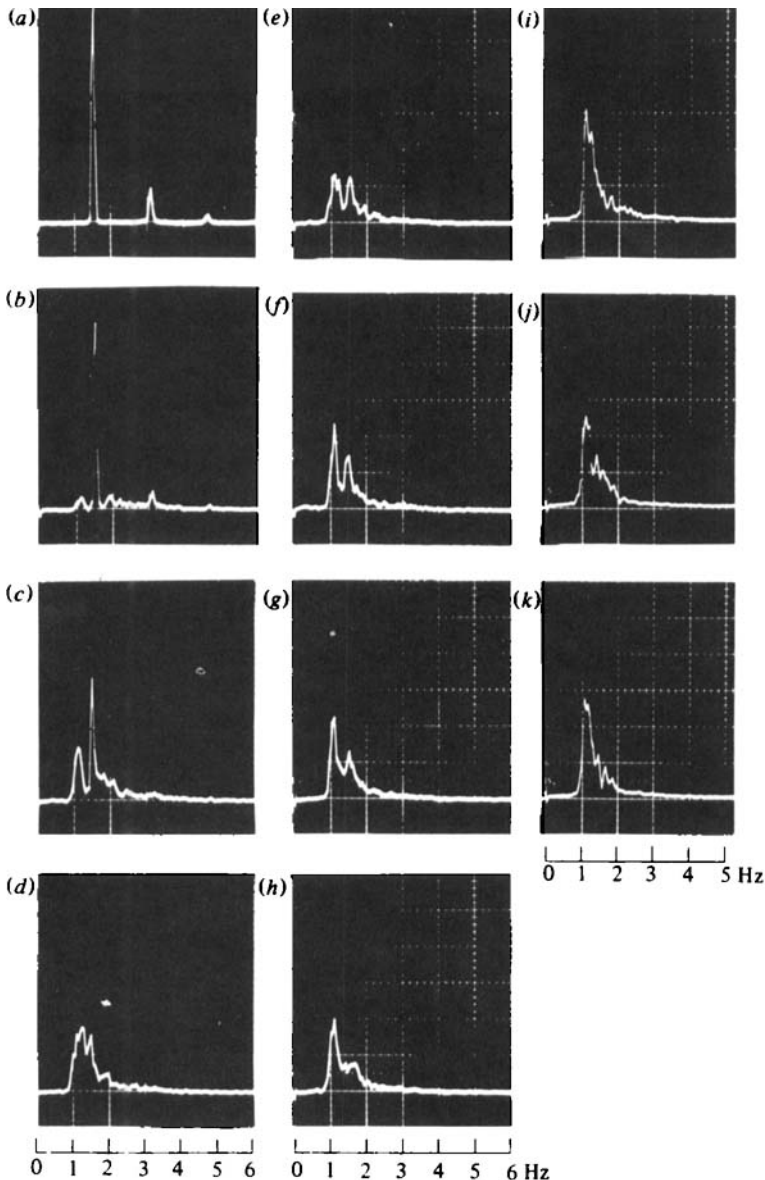


FIGURE 11. Evolution of power spectra corresponding to case B. (Note that the total energies from the different spectra cannot be compared directly, owing to the different calibration scales of the wave-height sensors.)

Some small cross-tank variations can be observed from these wave profiles, but are much smaller than the variation in the direction of wave train. These cross-tank variations may be due to reflections from the sidewalls of the tow tank of the oblique wave groups that are residues of the transformation from the three-dimensional breaking waves back to an essentially two-dimensional wave form (see §4 for more detail).

3.4. *Evolution of power spectra of surface displacement*

The power spectra corresponding to the four cases of wave forms with two different steepnesses, shown in §3.3, are calculated, with typical examples for cases B and A

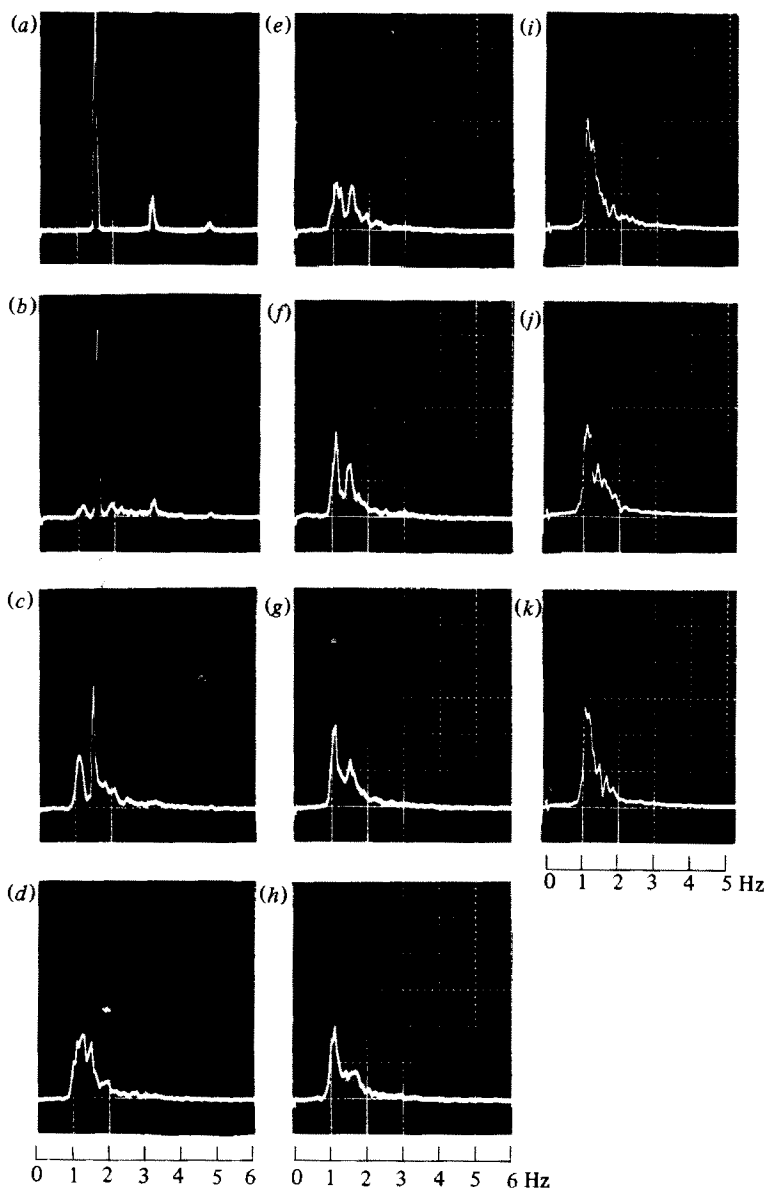


FIGURE 12. Evolution of power spectra for case A.

shown in figures 11 and 12. The spectra were computed directly from the voltage outputs from the wave gauges by an analog spectrum analyser that performs FFT internally, and displayed on a CRT and then photographically recorded. Because the calibration scales from different wave-height sensors at different locations are different, the total energy, which is equal to the area under each spectral curve, cannot be compared among different spectra in these figures.

For case B (figure 11) two sidebands of the Benjamin–Feir-type instabilities grow steadily from $x = 6.1$ m ($4.7\lambda_0$) to $x = 30.5$ m ($23.7\lambda_0$). The higher-frequency band contains more energy than the lower band. From $x = 36.6$ m ($28.7\lambda_0$) to 54.9 m ($42.4\lambda_0$), the trend of growth on two side bands reverses. From $x = 54.9$ m ($42.4\lambda_0$)

Case	F_0 (Hz)	λ_0 (m)	$H_0 = 2a_0$ (cm)	H_0/λ_0	$a_0 k_0$	f_1 (Hz)	f_0/f_1
A	1.55	0.61	0.62	0.101	0.32	1.15	1.35
B	1.05	1.295	10.3	0.0675	0.25	0.80	1.31
C	1.15	1.125	10.7	0.095	0.30	0.90	1.28
D	1.25	1.035	10.9	0.105	0.33	0.95	1.32

TABLE 1. Parameters used in experiments

to $x = 67.1$ m ($51.8\lambda_0$), the peak energy at initial frequency $f_0 = 1.05$ Hz decreases by about 50%, while a lower-frequency peak centred at $f_1 = 0.80$ Hz almost doubles in magnitude. This transition in the power spectrum corresponds to a marked transition in the wave forms.

In order to check whether the spectral shapes (such as the final examples in cases C and D) remain relatively unchanged, an additional case (table 1, case A) with $f_0 = 1.55$ Hz and $a_0 k_0 = 0.32$ is shown in figure 12. The initial wavelength $\lambda_0 = 0.61$ m for case A is much shorter than that (1.035 m) for case D; thus the effective length of evolution for case A in the same physical distance x will be longer. The three power spectra measured at $x = 76.3$ m ($73.7\lambda_0$), 91.5 m ($88.4\lambda_0$) and 107 m ($103\lambda_0$) respectively are seen to be approximately the same. In other words, the spectrum appears to reach an approximate equilibrium form. The speculation on the attainment of the spectral equilibrium remains to be checked by further experiments. (Note that the last three spectra in figure 12 were obtained and processed at a later time than the rest, and recorded in a different scale.)

Next we shall consider the ratio of the initial frequency f_0 to final peak frequency f_1 of an energy spectrum due to frequency downshifting for cases A–D. In table 1, the ratios of f_0/f_1 for cases A–D range from 1.28 to 1.35 and have an average of 1.32. This average ratio of frequency downshifting is very close to $4/3 = 1.33$. Of course, the above $f_0/f_1 = 4/3$ is the only dominant one. In cases C and D, $f_0/f_1 = 5/4 = 1.25$ and $3/2 = 1.5$ are present as well, but less frequently. Among these three modes of frequency downshifting, the experimental results show that the relative order of occurrence f_0/f_1 is $4/3$, $5/4$ and $3/2$.

The question of timescales of the frequency downshifting will be addressed next. Cases B and C each have a timescale of about 40 wave periods, while cases D and A both have a timescale of about 60 wave periods. This result is somewhat surprising at first glance: one would expect that the timescale for a steeper wave train would complete the strong interaction of frequency downshifting more rapidly. A likely explanation for this effect is given in §5. The example with $f_0 = 3.25$ Hz and $a_0 k_0 = 0.29$ (Lake *et al.* 1977) gives a timescale of about 50 wave periods, which is in the same range as our experimental results.

4. Results of experiments in the wave basin

4.1. General characteristics of wave evolution

We consider a representative example in which a wave train is generated with a plunger stroke of 5.1 cm, the basic frequency $f_0 = 1.55$ Hz and the wavelength $\lambda_0 = 65$ cm. The wave steepness $ak = 0.32$ measured at $x = 6.1$ m ($9\lambda_0$). Thus the initial wave conditions are the same as case A used in §3. For reference, figure 13

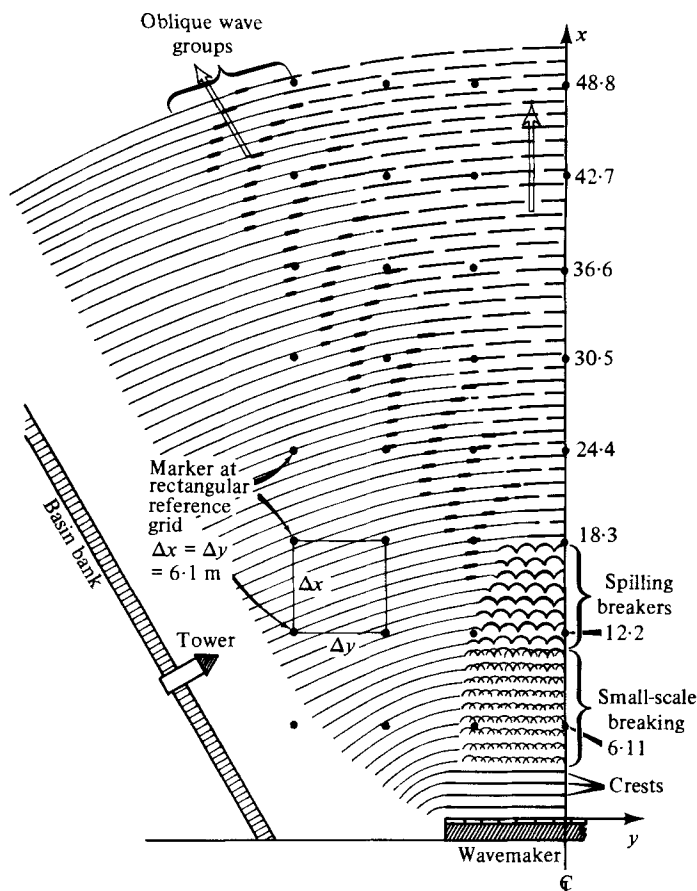


FIGURE 13. A sketch of overall characteristics of wave patterns for evolution of a steep wave train in the wave basin; $f_0 = 1.55$ Hz, $(ak)_0 = 0.32$.

depicts the overall characteristics of the wave patterns in the evolution of the steep wave train.

Figure 14 shows the wavemaker and the wave patterns up to $x = 15$ m ($23\lambda_0$). The first few waves are seen to contain small superharmonic disturbances, which grow in size and height. These perturbations are three-dimensional, with wavelength approximately equal to $\frac{1}{3}$ of the wavelength of the basic wave. The heights of these perturbations are larger on the crest than in the troughs of the underlying basic waves. The perturbations are first detected at the front face of the plunger A, which is composed of three approximately equal-length flat surfaces below the still-water level. The amplitudes of these perturbations reach their maxima at about $10\lambda_0$ from the wavemaker, where some small-scale breaking is obvious on crests of the longer primary waves.

Figure 15 shows the same wave pattern as figure 14, but the angle of incidence of the sunlight is lower; the presence of subharmonic modulation is more apparent under this condition. Starting from $x = 6.1$ m ($9\lambda_0$), we see that glitter created by superharmonic perturbations is accentuated at the higher wave crests, which alternate with lower, smoother crests for about ten wavelengths of the primary waves.

In the following phase of evolution the pattern changes to two high crests followed by two low crests (figure 14, left side). In figure 16 patterns are observed from the



FIGURE 14. The wavemaker and the wave patterns in the wave basin up to $x = 15.5$ m with $f_0 \approx 1.55$ Hz, $(ak)_0 = 0.32$. Picture is taken from a tower at 12 m above mean water surface. The expansion angle is $\theta \approx 17^\circ$.

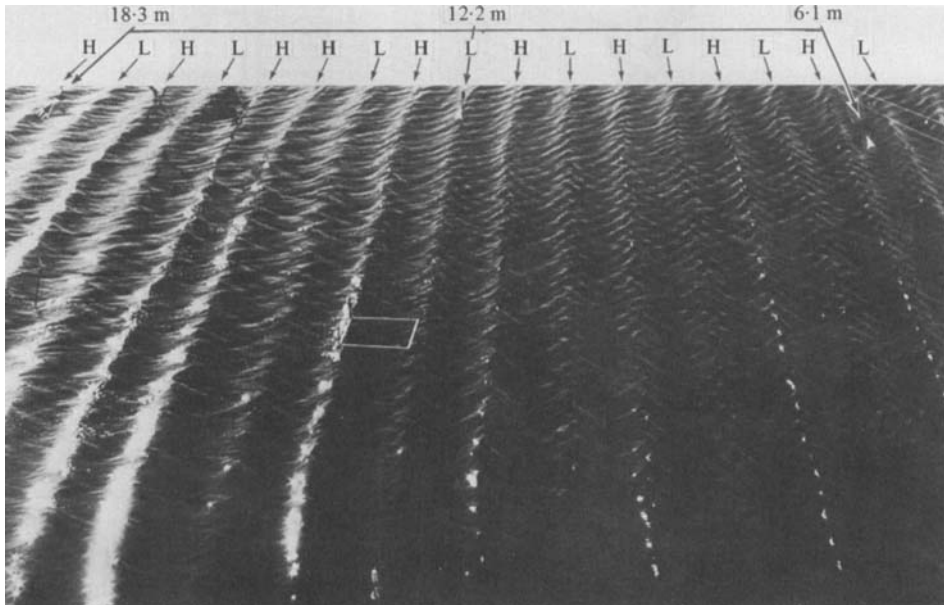


FIGURE 15. The same wave patterns as in figure 14 but taken at a much lower sun angle to show two-dimensional subharmonic instabilities.

centre of the wavemaker about 3 m above the still-water level. The three-dimensional characteristics of subharmonic modulation can be clearly seen from about $10\lambda_0$ to $30\lambda_0$ of the wavemaker.

Figure 17 is a close-up view of the three-dimensional spilling breakers due to subharmonic instabilities. These breakers occur around $15 \text{ m} \leq x \leq 25 \text{ m}$. The crescent-shaped breakers observed in the narrow tank and wide basin are quantitatively similar; consequently we surmise that the three-dimensionality of the spilling breakers is an intrinsic characteristic of the three-dimensional subharmonic instabilities.

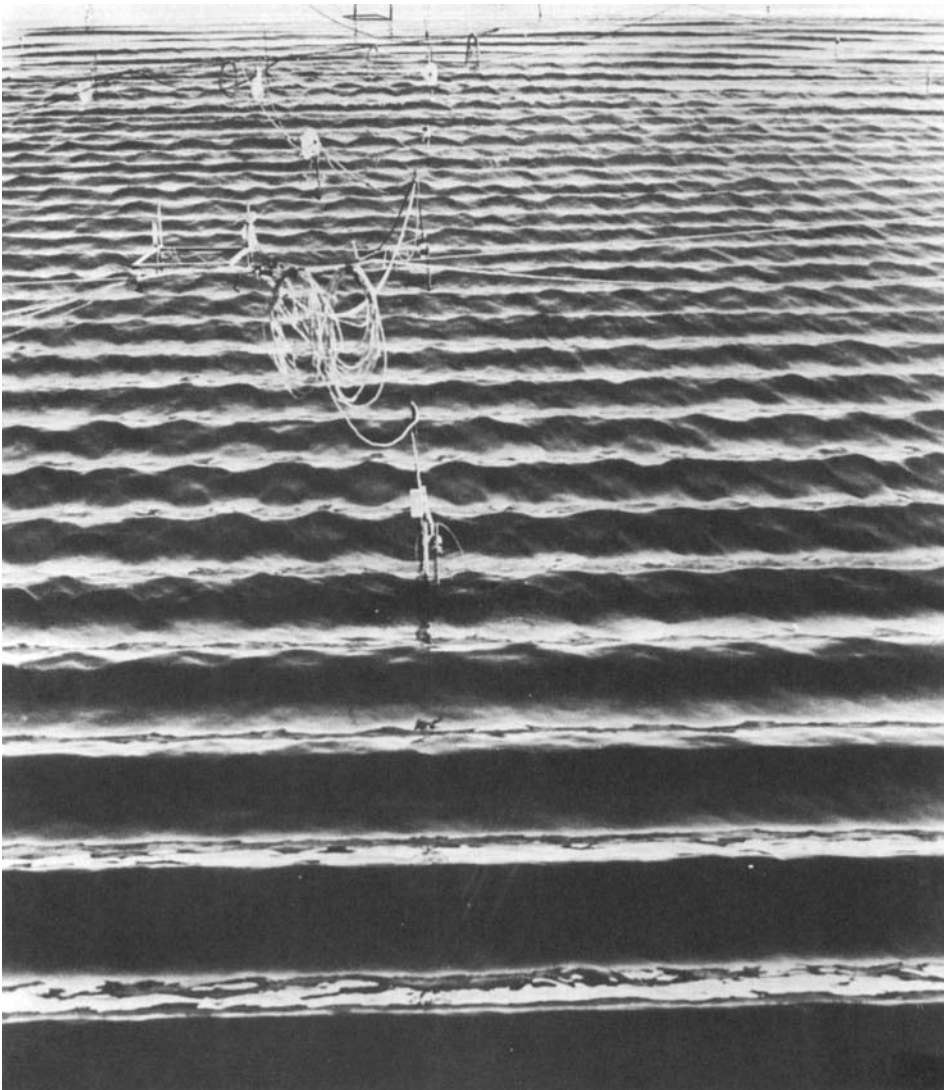


FIGURE 16. The same wave patterns as in figure 14 but viewed from the centre of the wavemaker and at 3 m above the water surface.

In the next phase (figure 18) the three-dimensionality of the patterns diminishes greatly, and long-crested waves dominate. We note that at the beginning of this phase a breaking wave appears on every third or fourth crest. Later the higher crests appear on the fifth, sixth or seventh waves. These features are consistent with those observed in the tow tank.

A new phenomenon that is not seen in the tank occurs in the wave patterns observed in the wide basin. This phenomenon appears to be related to the residues of the transition of the three-dimensional spilling breakers to the essentially two-dimensional wave forms, and provides a novel physical mechanism for directional energy spreading. It is believed that the above phenomenon also occurred in the tow tank; but was obscured by reflections from the sidewalls. An example of the phenomenon is given in figure 19, where a series of wave groups with about eight waves per group are shown propagating obliquely at a constant angle about 30° away



FIGURE 17. A close-up of three-dimensional spilling breakers in the wave basin around $x = 15$ m.



FIGURE 18. Wave patterns in the wave basin after the wave breaking.



FIGURE 19. Wave patterns at the final stage of the evolution starting in figure 14. The oblique wave groups due to three-dimensional wave breaking are propagating from the lower right corner to the upper left corner of the photograph.

from the basic wave direction; in the figure this phenomenon occurs along a strip extending from the lower right corner to the upper left. This feature persists for a distance of more than one hundred wavelengths.

Next, we shall address some possible effects that the finite crestlength of the plunger (15.85 m) may have on the three-dimensional evolution of the wave train described above. Figure 14 shows that the angle of expansion from the end of the plunger is about 17° . Thus, near the centreline at $x = 18.3$ m, waves with a crestlength ≈ 7.3 m contain most of the initial energy generated by the wavemaker. Beyond this range, the wave height decreases gradually outward. The decrease in wave height due to expansion causes the heights of crescent-shaped waves to vary along each crest.

4.2. Wave profiles and power spectra

The wave profiles taken along a line normal to the centre of the wavemaker were measured at eight stations (figure 20). The first four wave profiles (figure 20) near the wavemaker are highly repeatable from run to run. The other five wave profiles (figure 20) at greater distances are more variable, but the basic features are represented by these examples. At $x = 18.3$ m ($29\lambda_0$), the wave profile shows the increasing wave heights for alternate waves. The ratio of wave heights of consecutive waves is about 15/16, and the higher waves reach breaking points. The slopes of the forward faces become much larger than those at $x = 6.1$ m ($9\lambda_0$). At $x = 24.4$ m ($38\lambda_0$), every third wave becomes higher and some waves break. At $x = 30.5$ m ($47\lambda_0$), every

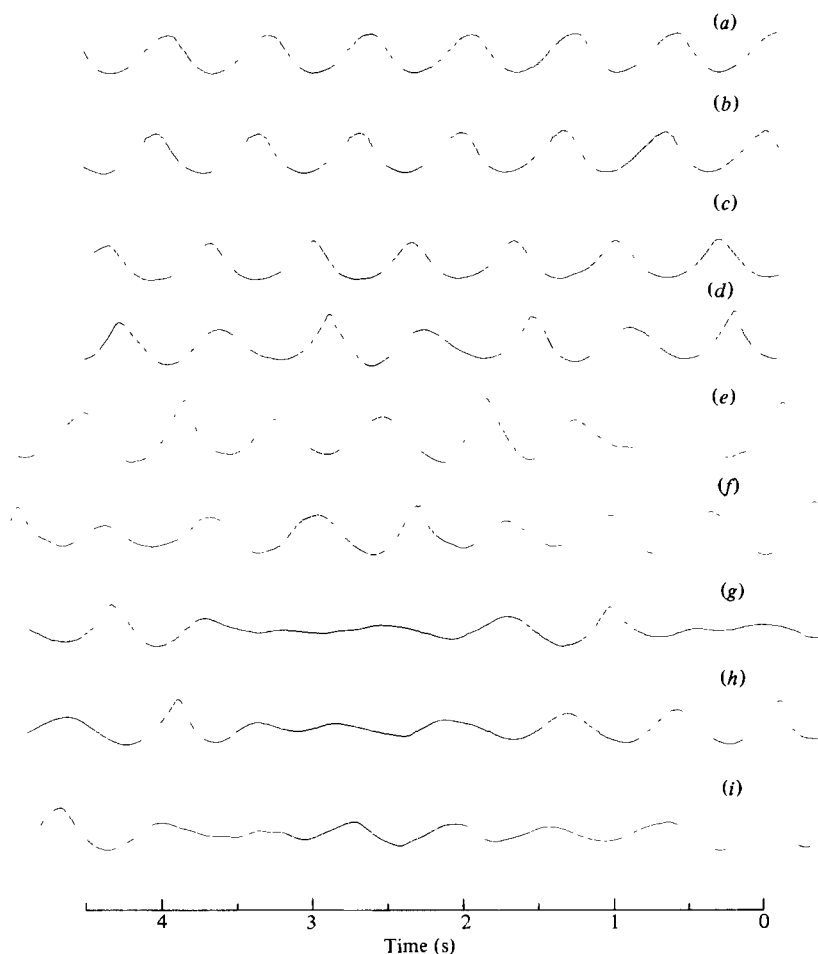


FIGURE 20. Wave profiles at various stages of wave evolution with the same condition as in figure 14. Locations of measurements are (a) 3.05 m; (b) 6.1 m; (c) 12.2 m; (d) 18.3 m; (e) 24.4 m; (f) 30.5 m; (g) and (h) 36.6 m; (i) 48.8 m.

fourth wave becomes steep enough to break. These examples indicate that the wave envelopes are asymmetric about the highest wave in the envelope. The deepest trough occurs at the rear face of the highest wave, in direct contrast with the three-dimensional spilling breaker, which has the deepest trough at its forward face.

As the wave evolution progresses, profiles at $x = 36.6$ m ($56\lambda_0$) and $x = 48.8$ m ($75\lambda_0$) show subharmonic modulations with even longer periods between amplitude maxima; i.e. every fifth, sixth, seventh wave respectively. We also note that some waves seem to disappear altogether. This phenomenon is due to the redistribution of energy during the process of subharmonic instability; some waves gain energy at the expense of the neighbouring waves.

The power spectra computed from the time series of the wave records at the stations in figure 20 are shown in figure 21. General characteristics of the spectral evolution in the wave basin are very similar to the tow-tank results, but the growth rate of the lower spectral peak at $f_0 = 1.15$ Hz is found to be smaller in the wave basin. This lower growth rate is to be expected, since significant wave-energy leakage occurs as a result of the expansion of the wave pattern at distances of the order of the plunger length.

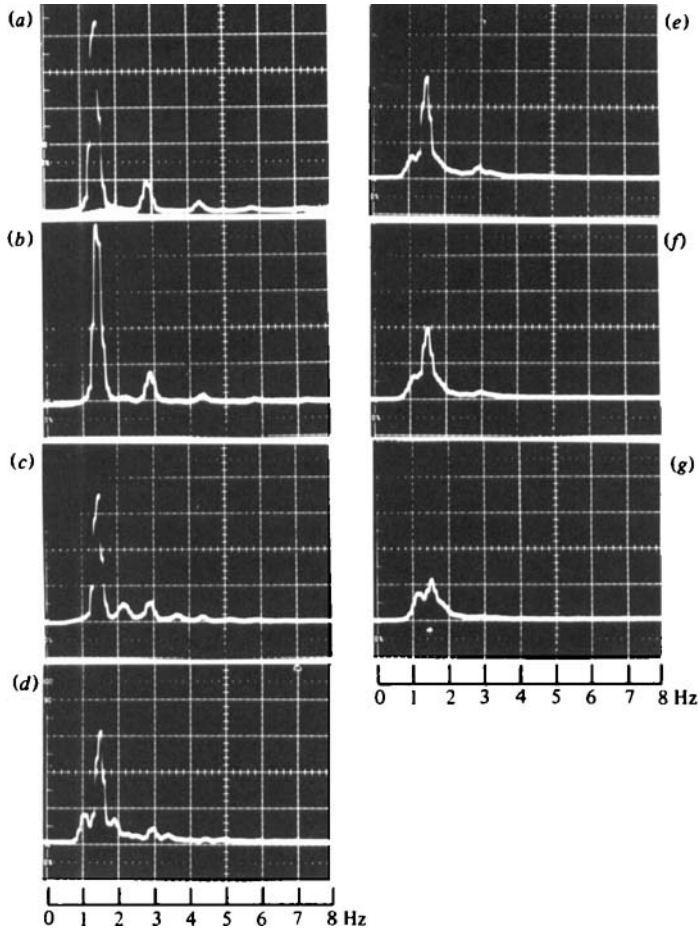


FIGURE 21. Evolution of power spectra associated with figure 20. Locations are (a) 6.1 m; (b) 12.2 m; (c) 18.3 m; (d) 24.4 m; (e) 30.5 m; (f) 36.6 m; (g) 48.8 m.

4.3. Comparisons of results of the wave-basin and tow-tank experiments

Results of observations and measurements in the wave basin and tow tank have notable similarities and differences. First, the experiments in the wave basin avoided two main effects of the sidewalls in the wave tank, i.e. viscous boundary layers on the walls and wave reflection. On the other hand, the experiments in the wave basin were affected by the wave diffraction from the ends of the plunger and energy leakage. These latter effects seriously limit the maximum distance along the centreline of the wavemaker for unbiased measurements of wave evolution. The maximum distance is about 50 m ($77\lambda_0$) for the 16 m crestlength of the wavemaker; this distance is only about $\frac{1}{3}$ of the total length (137 m) of the wave tank. Another possible drawback of the wave basin is its relative shallowness compared with the tow tank. The effective wavelength of subharmonic instabilities is much longer than that of the fundamental waves. Hence, strictly speaking, the wave evolution in the basin does not satisfy the deep-water approximation.

The essential characteristics of superharmonic and subharmonic instabilities, wave breaking and peak-frequency downshifting are consistently similar in both facilities, although both facilities have inherent limitations. The steep three-dimensional,

deep-water wave phenomena reported here are not artifacts of the experimental setups, but are the intrinsic nature of (mechanically generated) steep water waves. This experimental observation will be further supported by theoretical computations in §5.

Finally, the obliquely propagating wave groups, which are generated during the transition from three-dimensional breakers to less-steep two-dimensional wave forms, are observed only in the wide wave basin. Referring to figure 13, we see that these wave groups seem to originate from the geometric centre of the region where the wave-breaking occurs rather than from the centre of the plunger. Our experimental results provide an example of a physical mechanism that is based on three-dimensional instabilities of steep waves themselves.

5. Comparisons with theory

5.1. Wave breaking

A recent theoretical and numerical (linear-perturbation) analysis by McLean *et al.* (1981) and McLean (1982*a*) shows that there exists a new type (called type II) of instabilities, which are predominantly three-dimensional, in contrast with the well-known Benjamin–Feir type (called type I) instabilities, which are predominantly two-dimensional in nature. Type II are weaker than type I when $ak \leq 0.3$, but become much stronger when $0.3 < ak < 0.44$. The two-dimensional extremely fast-growing instability when $ak > 0.40$, first discovered by Longuet-Higgins (1978*a*), is a special case of the type II instability. Figure 22 shows two stability diagrams computed by McLean (1982*a*, figures 2*c*, *d*) for $ak = 0.30$ and 0.33 respectively. It should be noted that the maximum growth rate for type II instability occurs always at $p = 0.5$, i.e. with a perturbation wavelength equal to two unperturbed basic wavelengths. For $0.3 \leq ak \leq 0.33$, the corresponding q is $1.15 \leq q \leq 1.33$, i.e. the crestwise perturbation wavelength is slightly shorter than the basic wavelength. It seems to be most likely that the three-dimensional spilling breakers are due to the three-dimensional type II instabilities discussed by McLean *et al.* (1981) and McLean (1982*a*). Further discussion on three-dimensional steady wave patterns can be found in Su (1982) and Meiron, Saffman & Yuen (1982).

5.2. Frequency downshifting

Longuet-Higgins (1978*b*) has given a two-dimensional linear-perturbation analysis for all normal modes of instabilities of arbitrary wave steepness for deep-water gravity waves. This analysis includes subharmonic perturbations, with wavenumbers less than the fundamental waves. We shall use his example of $m = 8$; i.e. the perturbations with a repetition distance of eight fundamental wavelengths as one of the theoretical results. Figure 23 is extracted from his paper to show the real part of perturbation frequencies and corresponding growth rates respectively. In figure 23(*a*) a normal mode is denoted by $8n = 1, 2, 3, \dots, 15, 16$, which refers to the number of perturbed wavelengths in a period of eight unperturbed waves. In figure 23(*b*) a pair of normal modes that have the same growth rate is denoted by $8n = (r, s)$, with $r + s = 16$.

The mode of type I subharmonic instability underlying the frequency downshifting of $f_0/f_1 \approx 4/3$ is $8n = (4, 12)$ in figure 23, which is unstable for $0.23 < ak < 0.36$, and which has a maximum growth rate at $ak = 0.32$. This prediction is qualitatively consistent with the experimental observations (cases A, C and D) in which the

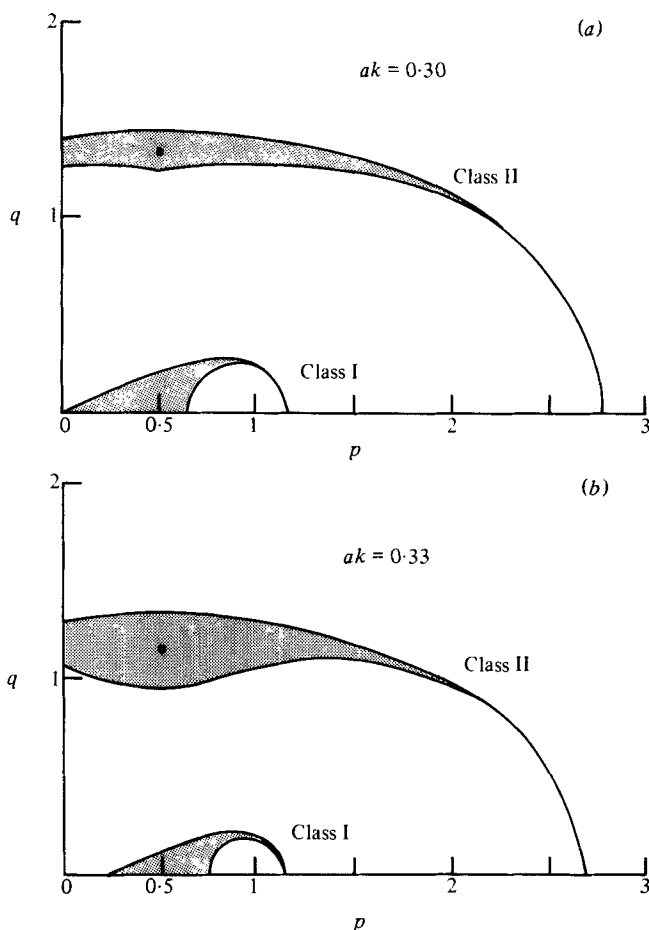


FIGURE 22. Instability regions of deep-water waves of finite amplitude. ● labels the point of maximum instability (from McLean 1982*a*, figures 2*c*, *d*). p and q are the perturbation wavenumbers along and transverse to the basic unperturbed two-dimensional waves.

alternate waves grow higher and lead to three-dimensional breaking. Subsequently, the $f_0/f_1 \approx 4/3$ frequency downshifting is observed.

In case C, with $a_0 k_0 = 0.30$, we observe the occurrence of the mode $f_0/f_1 \approx 5/4$, but less often than mode $f_0/f_1 \approx 4/3$. This observation can also be explained on the basis of growth rate of unstable modes.

In case D, with $a_0 k_0 = 0.33$, which is the maximum steepness in our experiments, we notice that groups with three waves (in figure 11, $x = 48.8$ m) are excited prior to groups with four waves (in figure 11, $x = 54.9$ m). This is probably due to the higher growth rate of the mode $f_0/f_1 \approx 3/2$ than that of mode $f_0/f_1 \approx 4/3$. As Longuet-Higgins (1978*b*) extended his normal-mode analysis to cover the complete continuous wave-steepness range (see his figure 7), the growth rate of the mode $f_0/f_1 \approx 3/2$ was between those of mode $f_0/f_1 \approx 8/5$, and $f_0/f_1 \approx 4/3$ at $a_0 k_0 = 0.33$.

If we rely only on the linear analysis of subharmonic instabilities (figure 23), we can ask the logical question as to why the mode (5, 11) with a larger growth rate than the mode (4, 12) at $a_0 k_0 < 0.28$ has not shown up in case B with $a_0 k_0 = 0.25$. In addition to the factor of growth rate, it is speculated (without proof at the present

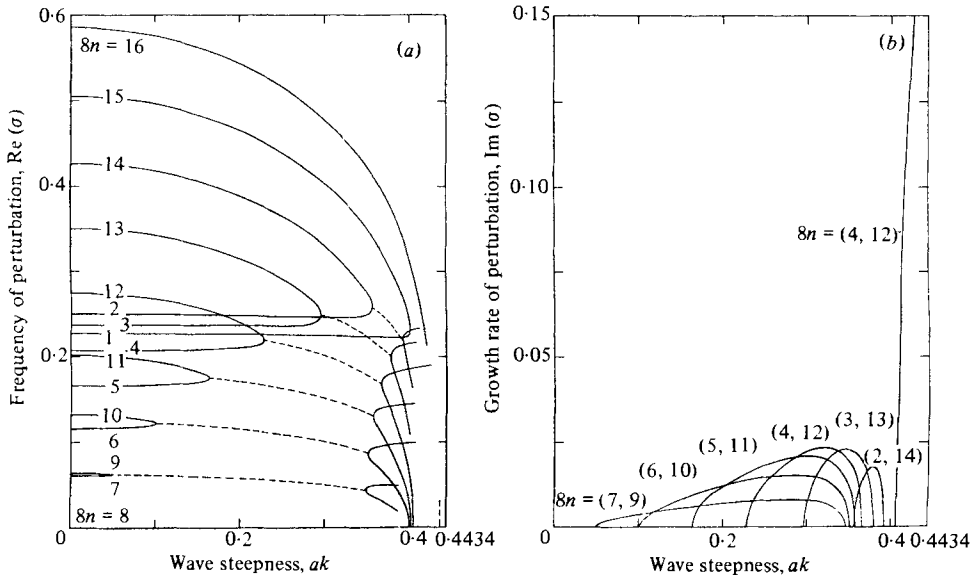


FIGURE 23. Frequencies (a) and growth rates (b) of subharmonic instabilities when $m = 8$ (from Longuet-Higgins 1978b).

time) that the maintenance of a coherent structure of a group of waves undergoing the strong interaction (frequency downshifting) is another important factor to influence selective excitation modes of nonlinear subharmonic instabilities. It is reasonable to say that the coherent structure of a wave group is easier to maintain for a group with a smaller number of waves. With $m = 8$, the minimal group for the mode (4, 12) is four waves (in time domain), while the minimal group for the mode (5, 11) is eight waves (in time domain); that is, the former is half as many. This could be the reason why we have observed predominantly the $f_0/f_1 \approx 4/3$, rather than $f_0/f_1 \approx 8/5$, frequency downshifting.

A typical example of the long-time evolution of an initially uniform steep wave train with $f_0 = 3.25$ Hz and $(ak)_0 = 0.23$ was given by Lake *et al.* (1977). Their figures 5 and 6 show the evolution of wave profiles and corresponding power spectra. The ratio of the carrier frequencies for the initial and final stages in this example is about 1.3. That is to say, there is as much as 25% downshift in the peak frequencies. Lake *et al.* (1977) and Yuen & Lake (1980) have attributed the phenomenon of seemingly returning to a more or less uniform wave train to be a water-wave analogy of the Fermi–Pasta–Ulam recurrence phenomenon. On the other hand, no explanation for the definite frequency downshifting has been offered by those authors.

Our experimental results have not only confirmed earlier observations by Lake *et al.*, but, more importantly, have established and identified the phenomenon of frequency downshifting as one of the most important characteristics of strong nonlinear interactions in the gravity waves in deep water.

6. Conclusions

A series of experiments on nonlinear evolution of deep-water gravity-wave trains with large steepness have been performed in a tow tank and a wide basin. Analyses of the experimental results with comparisons with available theories reveal the following general characteristics:

1. At an early stage of the evolution of these wave trains with $ak \geq 0.25$ the wave forms are essentially two-dimensional. At later stages, the growth of transverse perturbations causes a distinctly three-dimensional structure. Subsequently, the wave train evolves rapidly into rows of crescent-shaped spilling breakers, which are arranged with one half-breaker shifting between two consecutive rows. These breakers resemble spilling breakers found in open oceans.

2. After about ten wavelengths, these three-dimensional breakers transform just as quickly back to nearly two-dimensional long-crested wave forms. During this process, two series of oblique wave groups are formed and radiate symmetrically away from the primary wave direction at a constant angle of about 30° . These oblique wave groups appear to be residues of the three-dimensional spilling breakers, which cannot be transformed completely back to two-dimensional wave forms. These spilling breakers are examples of a source of directional spreading of wave energy, which has not been previously reported. These breakers are also a source of fine-scale turbulence in the surface layer and the momentum transfer from surface waves to mean currents.

3. Further evolution of the two-dimensional waves, after wave breaking, shows a distinct shift of the peak frequency of the energy spectrum towards lower frequency by as much as 25%. During this phase of evolution, the wave train becomes a series of wave groups (or packets) with much lower steepness and wave height than the initial stage. The downshift of wave frequency and decrease in steepness are the dominant characteristics of strong nonlinear interactions in deep-water gravity waves. These highly nonlinear processes provide a conceptual physical mechanism for energy and momentum transfers in narrow-band wave spectra, typically observed during rapid growth of ocean waves.

4. The three most frequently observed approximate modes of instabilities (for deep-water gravity-wave trains under subharmonic perturbations), in their order of frequency of occurrence, are close to $4/3$, $5/4$ and $3/2$ in terms of the ratio of basic unperturbed to perturbed frequencies. The preference for these unstable modes to other possibilities can be explained qualitatively by the linear analysis of subharmonic instabilities by Longuet-Higgins (1978*b*), and a novel postulation on maintenance of coherence of a wave group consisting of a smaller number of waves. The timescale for the $f_0/f_1 = 4/3$ frequency downshifting is about 40 to 60 fundamental wave periods for $0.25 \leq ak \leq 0.33$. This timescale is substantially shorter than the timescale normally accorded for the weak resonant wave-wave interaction.

5. Several important nonlinear dynamical processes in surface gravity subharmonic instabilities, wave breaking, directional energy spreading, turbulence generation, energy and momentum transfer among wave components, and others, appear to couple strongly in the continuous evolution of steep wave trains. These nonlinear processes are irreversible, but do not lead to complete randomness. Furthermore, these processes can occur only once for a given steep wave train, since the resulting wave steepness becomes too low to be able to undergo another strong nonlinear interaction.

6. The three-dimensional structures of waves during rapid transition due to strong nonlinear interactions suggest that the presently available models for wind-wave interaction do not accurately represent the pertinent physics, since they are fundamentally two-dimensional. It is our opinion that future models should incorporate the three-dimensional group characteristics of the wave field and the aerodynamics of turbulent air flow over the wave groups.

The senior author (M.Y.S.) is grateful to Professors W. H. Hui, M. S. Longuet-Higgins, E. Mollo-Christensen, O. M. Phillips, and P. G. Staffman, and Drs A. W.

Green and H. Yuen for helpful discussions and suggestions on various aspects of the study. The authors would like to thank the referee for a very detailed and constructive criticism of an earlier manuscript.

REFERENCES

- BENJAMIN, T. B. & FEIR, J. E. 1967 The disintegration of wave trains on deep water. Part 1. Theory. *J. Fluid Mech.* **27**, 417–430.
- HSU, Y.-H. L. 1976 A linear capacitance meter with applications to water wave measurements. Unpublished report, College of Marine Studies, University of Delaware, Newark, Delaware.
- LAKE, B. M., YUEN, H. C., RUNGALDIER, H. & FERGUSON, W. E. 1977 Nonlinear deep-water waves: theory and experiment. Part 2. Evolution of a continuous wave train. *J. Fluid Mech.* **83**, 49–74.
- LONGUET-HIGGINS, M. S. 1978*a* The instabilities of gravity waves of finite amplitude in deep water. I. Superharmonics. *Proc. R. Soc. Lond. A* **360**, 417–458.
- LONGUET-HIGGINS, M. S. 1978*b* The instability of gravity waves of finite amplitude in deep water. II. Subharmonics. *Proc. R. Soc. Lond. A* **360**, 489–505.
- LONGUET-HIGGINS, M. S. 1980 Modulation of the amplitude of steep wind waves. *J. Fluid Mech.* **99**, 705–713.
- LONGUET-HIGGINS, M. S. & COKELET, E. D. 1976 The deformation of deep surface waves on water. I. A numerical method of computation. *Proc. R. Soc. Lond. A* **350**, 1–36.
- LONGUET-HIGGINS, M. S. & COKELET, E. D. 1978 The deformation of deep surface waves on water. II. Growth of normal-mode instabilities. *Proc. R. Soc. Lond. A* **364**, 1–28.
- MCLEAN, J. W. 1982*a* Instabilities of finite-amplitude water waves. *J. Fluid Mech.* **114**, 315–330.
- MCLEAN, J. W. 1982*b* Instabilities of finite-amplitude gravity waves on water of finite depth. *J. Fluid Mech.* **114**, 331–341.
- MCLEAN, J. W., MA, Y. C., MARTIN, D. U., SAFFMAN, P. G. & YUEN, H. C. 1981 Three-dimensional instability of finite amplitude water waves. *Phys. Rev. Lett.* **46**, 817–820.
- MEIRON, D. I., SAFFMAN, P. G. & YUEN, H. C. 1982 Calculation of steady three-dimensional deep-water waves. *J. Fluid Mech.* **124**, 109–121.
- SU, M.-Y. 1982 Three-dimensional deep-water waves. Part 1. Experimental measurement of skew and symmetric wave patterns. *J. Fluid Mech.* **124**, 73–108.
- YUEN, H. C. & LAKE, B. M. 1975 Nonlinear deep-water waves: Theory and experiment. *Phys. Fluids* **18**, 956–960.
- YUEN, H. C. & LAKE, B. M. 1980 Instabilities of waves on deep water. *Ann. Rev. Fluid Mech.* **12**, 303–334.